Article

Modular Construction of Oxide Structures#Compositional Control of Transition Metal Coordination Environments

Christophe Tenailleau, Mathieu Allix, John B. Claridge, Maryvonne Hervieu, Michael F. Thomas, James P. Hirst, and Matthew J. Rosseinsky

J. Am. Chem. Soc., **2008**, 130 (24), 7570-7583 • DOI: 10.1021/ja077762f • Publication Date (Web): 28 May 2008

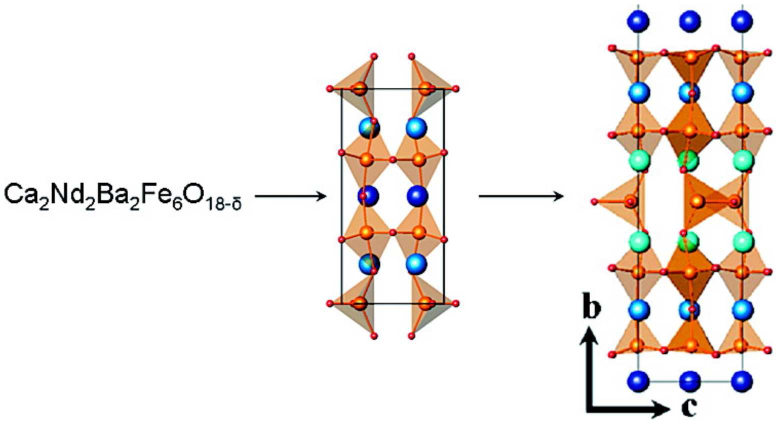

Journal of the American Chemical Society is published by the American Chemical Society. 1155 Sixteenth Street N.W., Washington, DC 20036

J|A|C|S
ARTICLES

Published on Web 05/28/2008

Modular Construction of Oxide Structures—Compositional Control of Transition Metal Coordination Environments

Christophe Tenailleau,[†] Mathieu Allix,[†] John B. Claridge,*[,†] Maryvonne Hervieu,[‡] Michael F. Thomas,[§] James P. Hirst,[†] and Matthew J. Rosseinsky*[,†]

Department of Chemistry, University of Liverpool, Liverpool, L69 7ZD, U.K., Laboratoire CRISMAT-ENSICAEN, UMR6508, 6 Bd du Maréchal Juin, 14050 Caen Cedex, France, and Department of Physics, University of Liverpool, Liverpool, L69 7ZE, U.K.

Received October 9, 2007; E-mail: claridge@liv.ac.uk; m.j.rosseinsky@liv.ac.uk

Abstract: The effects of reaction temperature and pO_2 were investigated on a series of (Ba,Ca,Nd)FeO$_{3-\delta}$ perovskite systems in order to isolate phases containing ordered arrangements of the distinct vacancy and cation ordering patterns identified in less compositionally complex iron oxide systems. Initial synthesis in air at high temperature yields cubic perovskite phases (**I**) with average iron oxidation states higher than 3; selected area electron diffraction together with diffuse features observed in the synchrotron X-ray diffraction (SXRD) patterns of these materials show evidence of small domains of short-range cation and vacancy order. Annealing these materials in nitrogen or in a sealed tube in the presence of an NiO/Ni buffer yielded the Fe^{3+} phase $Ca_2Ba_2Nd_2Fe_6O_{16}$ (**II**), closely related to $Sr_2LaFe_3O_8$ but with partial cation order as well as anion order present—the larger Ba cations are largely present in the 12-coordinate site between the octahedral iron layers, and Ca is largely present in 10-coordinate sites between octahedral and tetrahedral sites. Further reduction of $Ca_2Ba_2Nd_2Fe_6O_{16}$ using a Zr getter yields the mixed-valence phase $Ca_2Ba_2Nd_2Fe_6O_{15.6}$ (**III**). The structure of **III** was solved by maximum entropy analysis of XRD data coupled with analysis of high-temperature neutron diffraction data and refined against combined SXRD and high-Q ambient-temperature neutron data. This material crystallizes in a 20-fold perovskite super cell (*Imma*, a $\sim \sqrt{2}\times a_p$, b $\sim 10\times a_p$, c $\sim \sqrt{}\times 2a_p$) and can be visualized as an intergrowth between brownmillerite ($Ca_2Fe_2O_5$) and the $YBa_2Fe_3O_8$ structure. There are three distinct iron coordination environments, octahedral (O), square-pyramidal (Sp), and trigonal planar (Tp, formed by distorting the tetrahedral site in brownmillerite), which form a Sp−O−Tp−O−Sp repeat. Bond valence calculations indicate that Tp is an Fe^{2+} site, while the O and Sp sites are Fe^{3+}. The A-site cations are also partially ordered over three distinct sites: 8-coordinate between the Sp layers, 10-coordinate between Tp and O layers, and 12-coordinate between Sp and O layers. Mössbauer spectroscopy, magnetometry, and variable-temperature neutron diffraction show that the material undergoes two magnetic transitions at ∼700 and 255 K.

Introduction

Transition metal oxides are an important class of materials, with technological relevance in catalysis,[1] fuel cells,[2,3] displays,[4] sensors and actuators,[5,6] and communications and information storage technologies.[7] The bonding and electronic structure characteristics underpinning these properties also give rise to phenomena such as charge and orbital ordering[8] and multiferroic behavior.[9] One of the most important structures for applications, and among the most versatile for chemical tuning of composition and structure and thus properties, is the ABO_3 perovskite.[10] This structure has considerable capacity for compositional diversity, enabled by the ability to accommodate oxide anion vacancies[11] generated by variation of the cation charges on the A and B sublattices, which have coordination numbers of 12 and 6, respectively, in the stoichiometric undistorted cubic perovskite. The control of physical properties through A-site cation ordering is important in ionic and mixed conducting systems, where the mobility of oxide anions is strongly influenced by such order,[12,13] and in magnetism, where A-site-ordered $LaBaMn_2O_6$ has a significantly higher Curie temperature than the disordered

---

[†] Department of Chemistry, University of Liverpool.

[‡] Laboratoire CRISMAT-ENSICAEN.

[§] Department of Physics, University of Liverpool.

(1) Pena, M.; Fierro, J. *Chem. Rev.* **2001**, *101*, 1981–2017.

(2) Ruiz-Morales, J.; Canales-Vazquez, J.; Savaniu, C.; Marrero-Lopez, D.; Zhou, W.; Irvine, J. *Nature* **2006**, *439*, 568–571.

(3) Zhao, S. P.; Haile, S. M. *Nature* **2004**, *431*, 170–173.

(4) Ambrosini, A.; Malo, S.; Poeppelmeier, K.; Lane, M.; Kannewurf, C.; Mason, T. *Chem. Mater.* **2002**, *14*, 58–63.

(5) Saito, Y.; Takao, H.; Tani, T.; Nonoyama, T.; Takatori, K.; Homma, T.; Nagaya, T.; Nakamura, M. *Nature* **2004**, *432*, 84–87.

(6) Suchomel, M. R.; Davies, P. K. *Appl. Phys. Lett.* **2005**, *86*, 262905.

(7) Dawber, M.; Rabe, K.; Scott, J. *Rev. Mod. Phys.* **2005**, *77*, 1083–1130.

(8) Ronnow, H.; Renner, C.; Aeppli, G.; Kimura, T.; Tokura, Y. *Nature* **2006**, *440*, 1025–1028.

(9) Tokura, Y. *Science* **2006**, *312*, 1481–1482.

(10) Anderson, M. T.; Vaughey, J. T.; Poeppelmeier, K. R. *Chem. Mater.* **1993**, *5*, 151–165.

(11) Karen, P. *J. Solid State Chem.* **2006**, *179*, 3167.

(12) Kim, G.; Wang, S.; Jacobson, A. J.; Yuan, Z.; Donner, W.; Chen, C. L.; Reimus, L.; Brodersen, P.; Mims, C. A. *Appl. Phy. Lett.* **2006**, *88*, 1–3.

(13) Taskin, A. A.; Lavrov, A. N.; Ando, Y. *Appl. Phys. Lett.* **2005**, *86*, 091910.

10.1021/ja077762f CCC: $40.75 © 2008 American Chemical Society

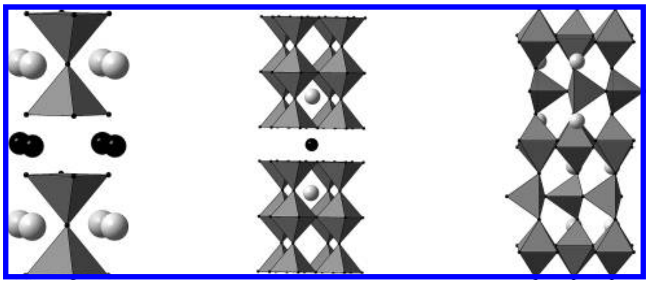

Figure 1. Crystal structures of $YBaFe_2O_5$,[16] $YBa_2Fe_3O_8$,[17] and $Ca_2Fe_2O_5$[18] featuring square-pyramidal, square-pyramidal plus octahedral, and octahedral plus tetrahedral coordination geometries.

$La_{0.5}Ba_{0.5}MnO_3$.[14] The spatial arrangement of the anion vacancies[15] at a given concentration often has a decisive influence on the selected physical properties, as the coordination environment and oxidation state of transition metals occupying the B site are controlled by vacancy ordering, as illustrated by the superconductivity of $YBa_2Cu_3O_{7-\delta}$, where the concentration and location of vacancies controls whether T_c is 90 K, 60 K, or 0 K. Although the geometry of the d-electron-bearing transition metal cations on the B site is often the focus of attention, vacancy ordering is frequently driven by the size-related coordination preferences of the A-site cations. This interplay between oxygen content, metal oxidation state, and A-site cation order produces a range of structures in Fe-based oxides; for example, $YBaFe_2O_5$,[16] $YBa_2Fe_3O_8$,[17] and $Ca_2Fe_2O_5$[18] feature square-pyramidal, square-pyramidal plus octahedral, and octahedral plus tetrahedral coordination geometries, respectively (Figure 1).

These cation- and vacancy-ordered units may themselves offer opportunities for the construction of more complex superstructures if they can be arranged by more detailed control of the A-site cation distribution. In this paper, the assembly of vacancy- and cation-ordered perovskite-based subunits into such superstructures is studied. We have selected Fe-based systems to investigate the synthesis of modular perovskite superstructures due to the variety of coordination environments possible for iron and the range of oxidation states (+2 to +4) accessible. The coupling between cation A-site and anion vacancy order observed in the known materials suggested the use of three A-site cations of differing size and charge in order to produce a single-phase material with A sites with distinct coordination environments. The importance of Ba and Ca in the three superstructures referred to above led to the selection of these cations in this study together with Nd^{3+}, which has a higher charge and forms a wider range of perovskites than the smaller lanthanides (e.g., Y^{3+}) but is more frequently involved in site ordering with divalent A cations than La^{3+}. The target was a superstructure containing tetrahedral, square-pyramidal, and octahedral B-site coordination geometries. $NdBaFe_2O_5$ and $Ca_2Fe_2O_5$ were selected as the base structural units because they contain the targeted coordination geometries. The exploration of the phase formation and structural chemistry began with reaction at compositions corresponding to the combination of $NdBaFe_2O_{5+\delta}$ and $Ca_2Fe_2O_5$ in ratios 1:1, 2:1, and 1:2 to discover compositions and oxygen contents lending themselves to the formation of such superstructures. Investigation of phase formation over a range of oxygen contents reveals a close interplay between oxidation state, A- and B-site coordination environment, and oxygen content that affords a 38 Å superstructure of perovskite with three distinct sites for both the A and B cations.

Experimental Section

Exploratory Synthesis. The 1:1, 1:2, and 2:1 combinations of the structural subunit materials $NdBaFe_2O_{5+\delta}$ and $Ca_2Fe_2O_5$ were explored by direct reaction of Nd_2O_3, $BaCO_3$, and $CaCO_3$ starting materials at the appropriate metal ratios over the 1000−1400 °C temperature range in air, flowing nitrogen, and flowing oxygen. Reactions were performed in alumina crucibles and boats with regrinding every two days over periods from 2 days to 2 weeks, with examination of products by powder X-ray diffraction (PXRD) at each regrinding step. Laboratory PXRD data were collected using both a Panalytical Xpert system using Co $K\alpha_1$ radiation in Bragg−Brentano geometry and a Stoe StadiP system using Cu $K\alpha_1$ radiation in Bragg−Brentano geometry. The precise conditions relevant to the specific samples will be given when they are discussed in the text. Thermal gravimetric analysis (TGA) was performed using a Seiko SII-TG/DTA 6300 thermal analyzer.

Synthesis of $Ca_2Ba_2Nd_2Fe_6O_{15+\delta}$. $Ca_2Ba_2Nd_2Fe_6O_{18-\delta}$ (Cubic Phase I). $CaCO_3$ (99.95%), $BaCO_3$ (99.997%), Nd_2O_3 (99.99%), and Fe_2O_3 (99.99%) powders were ground together in the required molar ratios, placed in an alumina boat, and fired at 1000 °C for 5 h and then at 1200 °C for 24 h. The black powder obtained was then well ground in order to ensure homogeneity of the sample before further reactions. Phases **II** and **III** (below) were formed from **I** initially by treatment in flowing N_2, as described in the Fe^{3+} $3a_p$ Phases and Isolation of the 10-Layer, $10a_p$ Phase **III** subsections in the Results section. This led to the development of the systematic synthesis routes described below.

$Ca_2Ba_2Nd_2Fe_6O_{16+\delta}$ (3 Layer, $3a_p$ Phase II). Phase **II** was formed by reduction of cubic phase $Ca_2Ba_2Nd_2Fe_6O_{18-\delta}$ (**I**) under vacuum, using the Ni/NiO couple as an oxygen buffer. The Ni/NiO couple could be achieved by starting with Ni metal only as the getter. Upon reduction of the sample, NiO was generated to create the Ni/NiO buffer. The metal reducer was placed at the bottom of a silica ampule to prevent any metal contamination of the sample when the ampule was opened after the reaction. The ampule was sealed under dynamic vacuum at 10^{-4} mbar before being heated to 1100 °C for 72 h. The product was a black sintered pellet.

$Ca_2Ba_2Nd_2Fe_6O_{15+\delta}$ (10-layer, $10a_p$ Phase III). This phase was originally identified by reaction of the cubic 1200 °C phase **I** at the 2:1 composition at 1150 °C for 3 days in a flowing nitrogen stream, gettered in the immediate sample environment by two Fe-filled alumina boats, with the aim of producing a lower oxygen partial pressure environment than for the initial flowing-gas synthesis of **II** discussed above. The final step in the more-controlled sealed-tube synthesis of **III** is a second reduction of Ni-reduced $Ca_2Ba_2Nd_2Fe_6O_{16+\delta}$ (**II**) by O_2-gettering under vacuum, using Zr metal as the getter in quantities corresponding to the O_{15} composition. The same setup as that for Ni/NiO oxygen buffering was used, and the reaction was carried out at 1100 °C for 72 h. The final compound was still black and very well sintered. Two different samples were synthesized. The first sample (≅0.5 g) was used for synchrotron X-ray diffraction (SXRD) collection and ambient-temperature neutron powder diffraction at ISIS, whereas a larger sample (≅2.5 g) was synthesized for collection of neutron powder diffraction data. During our experiments, the first sample appeared to be purer than the second one.

---

(14) Caignaert, V.; Millange, F.; Domenges, B.; Raveau, B.; Suard, E. *Chem. Mater.* **1999**, *11*, 930–938.

(15) Hadermann, J.; van Tendeloo, G.; Abakumov, A. M. *Acta Crystallogr. A* **2005**, *61*, 77–92.

(16) Karen, P.; Woodward, P. M. *J. Mater. Chem.* **1999**, *9*, 789–797.

(17) Karen, P.; Kjekshus, A.; Huang, Q.; Lynn, J. W.; Rosov, N.; Sora, I. N.; Karen, V. L.; Mighell, A. D.; Santoro, A. *J. Solid State Chem.* **1998**, *136*, 21–33.

(18) Berastegui, P.; Eriksson, S. G.; Hull, S. *Mater. Res. Bull.* **1999**, *34*, 303–314.

Transmission Electron Microscopy. Samples for transmission electron microscopy (TEM) were prepared by crushing the powder in *n*-butanol and depositing the small crystallites in suspension onto a holey carbon film, supported by a copper grid. The electron diffraction (ED) study was carried out with a JEOL 2000FX electron microscope. Energy-dispersive spectroscopy (EDS) analyses were systematically carried out during the ED study, the JEOL 2000FX being equipped with an EDAX analyzer. High-resolution electron microscopy (HREM) was performed with a TOPCON 002B microscope operating at 200 kV and having a spherical aberration constant $C_s = 0.4$ mm. The HREM theoretical images were calculated using the Mac-Tempas multislice program,[19] varying the focus values and crystal thickness and using the atomic positions obtained from the powder refinements carried out at room temperature.

Synchrotron X-ray Powder Diffraction. XRD experiments on phase **III** were performed on station 9.1 of the Synchrotron Radiation Source (SRS) at Daresbury Laboratory in the UK using $\lambda = 0.96605$ Å, with the sample contained in a 0.5 mm capillary. Data of quality suitable for Rietveld refinement were collected at room temperature over the 2θ range of 1−50°. Rietveld analysis was carried out on the XRD data using the GSAS software package[20] with the EXPGUI interface.[21] Maximum entropy electron densities were obtained using RIETAN2000 and PRIMA.[22–25] Data were collected on the ID31 beamline at ESRF using $\lambda = 0.495824$ Å on samples of **I** and **II** to identify weak superstructure reflections not visible in laboratory diffraction.

Maximum entropy methods (MEM)[24,26] were used in the structure solution of **III** to avoid the effect of termination due to unobserved peaks, which produce spurious features, making it difficult to extract physically meaningful residual electron density distribution maps from traditional Fourier synthesis methods of extracting electron densities from powder data. In this approach, rather than performing a Fourier transformation of the F_{obs} structure factors as obtained from Rietveld refinement by apportioning the intensity of overlapping observed reflections according to the calculated structure factors (difficult to perform for powder data owing to the collapse of reciprocal space onto a one-dimensional diffraction pattern and the resulting partial or complete overlap of Bragg reflections), a density distribution is estimated, and the information entropy is maximized within the errors of the observed data. Thus, MEM can be seen in some ways as the opposite of a Fourier synthesis, as an initial density is fitted to the observed scattering factors. (It is customary to start from a homogeneous density distribution.) As unobserved high-Q peaks do not affect the density, accurate electron densities can be obtained from limited numbers of integrated intensities.[24,27,28] The detailed theory of MEM is covered in the cited references. The use of MEM alone still maintains the F_{obs} as obtained from the initial extraction and is therefore biased toward the model used to extract the data. However, the results of an MEM calculation can be used to provide F_{calc} for a second extraction of F_{obs} from the observed data, which will be less biased toward the original model. Repeated extractions and MEM calculations should therefore yield the true scattering density. This cycling of the MEM results has been implemented in RIETAN-2000 by Izumi, who has applied the so-called REMEDY cycles to a number of diffraction problems.[23]

Powder Neutron Diffraction. Ambient-temperature data were collected on the first sample of phase **III** on the GEM diffractometer at ISIS Rutherford Appleton laboratory. Data over the *d*-spacing range 1.55 Å > *d* > 0.55 Å was used in the Rietveld analysis. Variable-temperature data were collected on the second sample of phase **III** at the Institut Laue Langevin on the D20 instrument from 5 to 773 K ($\lambda = 1.3$ Å). Following these measurements, because no magnetic reflections were visible above 700 K, data suitable for Rietveld refinement of the nuclear structure were recorded at 773 K on the D2B diffractometer ($\lambda = 1.5943$ Å).

Partial cation ordering over the three different A sites in **III** is obtained from combined analysis of the X-ray and neutron data. On one hand, because the X-ray scattering lengths of Ba and Nd are similar and considerably different from those of Ca, it was possible to refine the Ca composition on the different A sites versus a mixed (Ba,Nd) composition considered to be Nd-only in the X-ray refinement ($f(\mathrm{Ca}^{2+}) = 18$; $f(\mathrm{Ba}^{2+}) = 54$; $f(\mathrm{Nd}^{3+}) = 57$). On the other hand, the neutrons allowed us to distinguish Nd from a mixed (Ca,Ba) composition which we considered to be Ca in the neutron-only refinement. It is not possible to directly combine refinement of the X-ray and neutron diffraction data because they were not recorded at the same temperature, but it is possible to use a set of simultaneous equations (Table S4, Supporting Information) to determine the site occupancies, assuming that the cation order does not change between 298 and 773 K.

Titration. The oxygen content of **III** was determined using cerimetric titration. To prevent oxidation of the reductant by atmospheric oxygen, an acidic solution was used as a solvent and the titration medium was freed from dissolved oxygen before each experiment by Ar bubbling. About 50 mg of the sample was dissolved in 50 mL of water and 50 mL of concentrated HCl. The dissolution was aided by ultrasound irradiation. The resulting solutions were complexed with 50 mL of concentrated phosphoric acid and titrated under Ar with ferroin as an indicator against 0.1 M $\mathrm{Ce(SO_4)_2 \cdot 4H_2O}$ (BDH).

Mössbauer. The ^{57}Fe Mössbauer spectra were recorded on the first sample of **III** at 298 and 77 K with a constant acceleration spectrometer. The ^{57}Fe Mössbauer chemical isomer shift data are quoted relative to metallic iron at room temperature.

Magnetism. Magnetization measurements were carried out with a Quantum Design MPMS SQUID magnetometer. Magnetization data were recorded versus temperature from 2 to 300 K in applied fields of 500 or 100 Oe. Direct current magnetization hysteresis loops were recorded at 77 and 300 K with the field swept between ±50000 Oe. The sample was contained within a gelatine capsule fixed at the midpoint of a straw. The second sample of **III** was used for magnetic measurements.

Results

Cubic Phases. The initial exploratory reactions in air at all three compositions produced materials that were cubic to laboratory X-ray powder diffraction. The 2:1 $\mathrm{Nd_2Ba_2Ca_2Fe_6O_{18-\delta}}$ (**I**) composition prepared at 1200 °C in air for 55 h is shown by TGA reduction in dilute hydrogen at 1100 °C to have the oxygen content $\mathrm{Nd_2Ba_2Ca_2Fe_6O_{17}}$ ($\mathrm{Fe^{3.3+}}$), consistent with the ratios of the two observed Mössbauer resonances at $\delta = 0.32(2)$ (31% $\mathrm{Fe^{4+}}$) and $\delta = 0.148(4)$ (octahedral $\mathrm{Fe^{3+}}$, 69%) (Figure S1, Supporting Information). EDS analysis confirms the target cation composition is maintained.

Synchrotron data show **I** is metrically cubic with $a = 3.8850(3)$ Å. However, selected area electron diffraction shows

---

(19) Kilaas, R. *Mactempas*; Total Resolution LLC: Berkeley, CA, 2003.

(20) Larson, A. C.; Von Dreele, R. B. *General Structure Analysis System (GSAS)*, Report LAUR 86-748; Los Alamos National Laboratory: Los Alamos, NM, 2000.

(21) Toby, B. H. *J. Appl. Crystallogr.* **2001**, *34*, 210–213.

(22) Izumi, F. *J. Ceram. Soc. Jpn.* **2003**, *111*, 617–623.

(23) Izumi, F. *Solid State Ionics* **2004**, *172*, 1–6.

(24) Izumi, F.; Kumazawa, S.; Ikeda, T.; Hu, W. Z.; Yamamoto, A.; Oikawa, K. *Epdic 7: European Powder Diffraction, Parts 1 and 2*; Trans Tech Publications Ltd: Zurich-Uetikon, 2001; Vol. 378-3, pp 59−64.

(25) Xiao, Y. N.; Izumi, F.; Graber, T.; Viccaro, P. J.; Wittmer, D. E. *Powder Diffraction* **2003**, *18*, 32–35.

(26) Battle, P. D.; Gibb, T. C.; Lightfoot, P. *J. Solid State Chem.* **1990**, *84*, 237.

(27) Hadermann, J.; Abakumov, A. M.; D'Hondt, H.; Kalyuzhnaya, A. S.; Rozova, M. G.; Markina, M. M.; Mikheev, M. G.; Tristan, N.; Klingeler, R.; Buchner, B.; Antipov, E. V. *J. Mater. Chem.* **2007**, *17*, 692–698.

(28) Abakumov, A. M.; Kalyuzhnaya, A. S.; Rozova, M. G.; Antipov, E. V.; Hadermann, J.; Van Tendeloo, G. *Solid State Sci.* **2005**, *7*, 801–811.

complex patterns with diffuse streaking along the equivalent $[100]_p$* directions (the suffix p referring to the parameter a_p of the simple cubic perovskite cell), together with the local appearance of elongated nodes (Figure S2, Supporting Information). These features, also present in the ED patterns of the other two (1:1 and 1:2) compositions after the initial reaction in air, are consistent with the formation of small domains of short-range cation and vacancy order, with local stabilization of incommensurate (Figure S2a and enlargement showing nodes at 0 $^{2}/_{5}$ 0) and commensurate superstructures indicated by the nodes at 0 $^{1}/_{2}$ 0 (Figure S2b, $2a_p$ supercell), 0 $^{2}/_{5}$ 0 (Figure S2c, $3a_p$ supercell), and $^{1}/_{2}$ $^{1}/_{2}$ 0 (Figure S2d) due to an orthorhombic distortion of the $3a_p$ phase (see the discussion of **II** later). The incommensurate satellites could be associated with microphases built up from the $2a_p$ and the $3a_p$ domains. This ED evidence demonstrates that short-range ordering induced by the A cation size and charge differences occurs even in structures which are cubic to X-ray powder diffraction. The remainder of this paper focuses on the 2:1 composition of **I**, as it proved easier to extend the correlation lengths of these ordering features into well-defined superstructures at this composition than for the 1:1 and 1:2 ratios of the structural modules. The role of the cubic **I** phases here is to act as precursors for the subsequent chemistry, but it should be noted that the iron oxidation states above 3+ give rise to a series of charge disproportionation transitions, leading to the formation of Fe^{5+} (Figure S3, Supporting Information).

Fe^{3+} $3a_p$ Phases. The Fe^{3+} composition expected for the $3a_p$ supercell composition $Nd_2Ba_2Ca_2Fe_6O_{16}$ is attained by treatment of the cubic air-synthesized precursors in lower oxygen partial pressure. Annealing the 2:1 1200 °C cubic precursor **I** $Ca_2Nd_2Ba_2Fe_6O_{17-\delta}$ in flowing nitrogen for two weeks at 1150 °C produces a phase **II** with a b axis of $3a_p = 11.7$ Å and a structure related to Sr_2LaFe_3O8 (Figure 2a) with an octahedron−octahedron−tetrahedron (OOT) sequence of two octahedral layers followed by one tetrahedral layer. EDS analyses show the cation stoichiometry is maintained. XRD data are refined in the *Pmma* space group (Table S1, Supporting Information), shown by ED (Figure S5, Supporting Information). The oxide anion positions, when refined according to the $Sr_2LaFe_3O_8$ structure, have unrealistically large displacement parameters: inspection of difference Fourier maps from the SXRD data resulted in the identification of two anion positions displaced from the original and two tetrahedral iron sites, revealing the existence of two disordered orientations of regular tetrahedra (Figure 2b), as observed in several brownmillerite oxides.[29–31] A-site cation ordering is observed, with barium almost exclusively located on the larger site between the octahedral layers when the required assumption of an even Nd distribution over both sites is made (Table S1a and refinement in Figure S6b, Supporting Information). In the [001] HREM image (Figure 2c), the contrast consists of three rows of white spots, spaced by 11.5 Å along b and 2.7 Å along a, in agreement with the presence of the mirror a. Figure 2d shows adjacent [001] and [100] twinning domains; one defect (indicated by a horizontal bracket), consisting of a slice of two polyhedra instead of the three found in the regular structure, is visible between the two domains. The existence of defective slices with a thickness different from $3a_p$ is responsible for the diffuse phenomena along the b* axis, and such defects involving combination of $2a_p$ and $3a_p$ can be viewed as premonitory to the formation of the superstructure **III** discussed later.

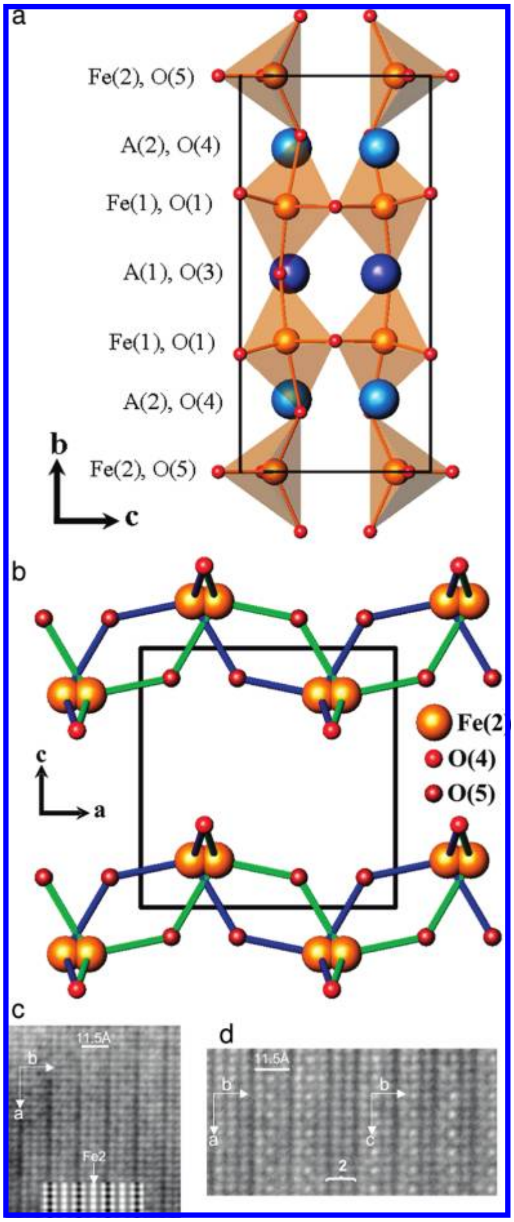

Figure 2. (a) Octahedral−octahedral−tetrahedral $3a_p$ trilayered structure of $Ca_2Nd_2Ba_2Fe_6O_{16}$ (**II**, $b = 11.7$ Å). The two different A cation sites are distinguished by shading. The darker site is rich in Ba. (b) Positional disorder in the tetrahedral layer of **II** is refined, resulting in a regular geometry (Figure S4 and Table S1b, Supporting Information) of the refined tetrahedra produced by selecting the green or blue sets of bonds around the iron site. (c) HREM image and simulation of **II** (inset). The contrast variation along b is associated with the rows of iron polyhedra, as confirmed by the inserted calculated image (focus value close to 0 and crystal thickness close to 28 Å using coordinates and site occupancies from Table S1a), the middle line of the bright dots corresponding to the Fe2 rows as indicated by the arrow. (d) Twin domains within the structure of **II**. The domains are [001] (left) and [100] (right) oriented as a result of the orthorhombic distortion of the cell. In the [100] area, bright and less-bright dots alternate along c, with a periodicity of 5.6 Å, as a result of the presence of the mirror m. The bracket indicates a defect with two rather than three Fe centers in the repeat.

The Fe^{3+} composition of the material **II** is consistent with Mössbauer measurements (Figure S6a) at 300 K, which show magnetic order with 75% $\delta = 0.36$ octahedral Fe^{3+} and 25% δ

---

(29) Abakumov, A. M.; Alekseeva, A. M.; Rozova, M. G.; Antipov, E. V.; Lebedev, O. I.; Van Tendeloo, G. *J. Solid State Chem.* **2003**, *174*, 319–328.

(30) Karen, P.; Suard, E.; Fauth, F. *Inorg. Chem.* **2005**, *44*, 8170–8172.

(31) Herrmann, D. B. M. *Mater. Res. Bull.* **1971**, 6.

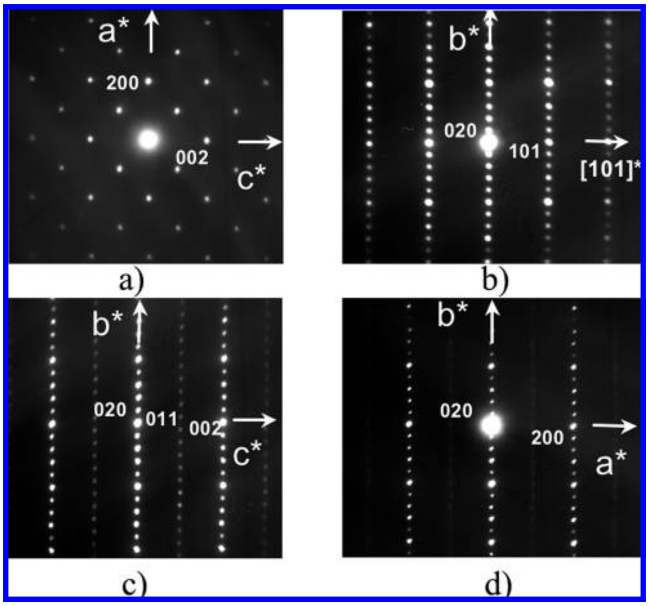

Figure 3. Experimental (a) [010], (b) [−101], (c) [100], and (d) [001] electron diffraction patterns of the $Ca_2Ba_2Nd_2Fe_6O_{15.6}$ oxide **III**.

= 0.22 tetrahedral Fe^{3+}. This excess of octahedral Fe is consistent with the regions of cubic defects revealed in SXRD data as intergrowth of the $3a_p$ phase with cubic perovskite. To isolate defect-free samples of **II**, the pO_2 ambient during synthesis was controlled in sealed tubes with metal/metal oxide couples at 1100 °C. Fe/FeO ($pO_2 = 3.9 \times 10^{-14}$ atm) gave decomposition to reduced ternary iron oxides and $NdCaFeO_4$. Co/CoO ($pO_2 = 2.64 \times 10^{-10}$ atm), Ni/NiO ($pO_2 = 1.4 \times 10^{-7}$ atm), and Cu/Cu_2O ($pO_2 = 5.9 \times 10^{-6}$ atm) couples all afforded material with the target $3a_p$ structure, with minimal impurities present in the Ni case. This procedure allows the iron oxidation state to be fixed at 3+ without the problems of adventitious impurities which are present in flowing gas reactions, permitting reduction from the O content which affords cubic vacancy-disordered material in the 1200 °C air-annealed cubic material **I**.

Isolation of the 10-Layer, 10*a*$_p$ Phase III. Larger supercells are accessible from the ordering of a higher concentration of anion vacancies in a manner identified in detail in the Experimental Section which gave initial access to the $10a_p$ phase **III**. Electron diffraction revealed a large supercell (Figure 3), confirmed by high-resolution SXRD data. Detailed electron microscopy revealed that the cation composition was accurate at $Nd_2Ba_2Ca_2Fe_6$ and that the sharp superstructure reflections have extinctions for $h + k + l = 2n$ and $hk0$: $h = 2n$ consistent with the space groups *Imma*, *Immb*, *I*2*mb*, and *Im*2*a*. The cell parameters $a = a_p\sqrt{2} \cong 5.5$ Å, $b = 10a_p \cong 38$ Å, and $c = a_p\sqrt{2} \cong 5.6$ Å, correspond to a 20-fold enlargement of the perovskite unit cell of **I**. The synchrotron data indicated that this supercell coexisted with a minority phase with the $3a_p$ superstructure in this sample. The $10a_p$ superstructure (referred to as “10-layer” in what follows) lines were observed in 1:1 and 2:1 samples treated in an analogous manner (Figure S7, Supporting Information) but were considerably broader, consistent with a reduced correlation length for ordering of the bilayer and trilayer components.

Isolation of a pure sample of this $10a_p$ material, referred to as **III**, proved difficult. Sealed-tube reactions with pO_2 fixed by the metal/metal oxide couples described above over a range of temperatures resulted either in total reduction, with decomposition of the perovskite structure, or in the Fe^{3+} $3a_p$ material. Investigation of the original sample of **III** after standing in air for several months reveals that the $10a_p$ superstructure reflections completely disappear, whereas the $3a_p$ ones remain. These combined observations indicate that the main problem in successfully isolating **III** is obtaining the correct oxygen content, with the air sensitivity presumably resulting from reduction from Fe^{3+} in the $10a_p$ material; the resulting $3a_p$ material is less crystalline than those directly prepared at high temperature.

An extensive exploration of target anion composition and reduction temperature using the zirconium gettering method allowed the isolation of **III**. This technique allows fixed amounts of oxygen to be removed from a starting material whose oxygen content is known. The variable oxygen content of the Fe^{4+}-rich cubic starting materials **I** makes them unsuitable starting materials for such an approach, but the precisely Fe^{3+} $3a_p$ phases **II** described above are well-suited as precursors. Exploration of a range of temperatures and compositions leads to identification of the $Nd_2Ca_2Ba_2Fe_6O_{15}$ composition (formed in a gettering reaction at 1100 °C), corresponding to an iron oxidation state of +2. This material has an X-ray pattern (entirely different from that of the $3a_p$ phase) which can be successfully fitted in a pattern-matching procedure with the $10a_p$ *Imma* structure of **III**—the low-angle reflections, in particular the (004), due to the superstructure are readily identifiable. The amount of $3a_p$ phase present in this material increases with time of exposure to air, and thus the $10a_p$ phase **III** requires handling as an air-sensitive material. Higher O contents produce a mixture of the $10a_p$ and $3a_p$ phases; lower oxygen contents result in the $10a_p$ phase and what appear to be non-perovskite decomposition products. Similar instability on either side of the correct oxygen content has been noted in the synthesis of $YBa_2Fe_3O_8$.[32]

Structural Characterization of the 10-Layer, 10*a*$_p$ Phase III. Detailed investigations with TEM, neutron and X-ray diffraction, and Mössbauer spectroscopy were performed to identify the iron coordination environments and derive a structural model for **III**. The pure material was well-crystallized upon TEM examination, with ED patterns similar to those presented in Figure 3 and reconstruction of the reciprocal space by tilting around the *b** axis giving the same systematic absences and possible space groups.

Numerous crystals were selected in order to determine the actual cationic composition of **III**. The composition was found to be slightly different from that in the starting material: $Ca_{1.88}Ba_{1.92}Nd_{2.22}Fe_6$, in contrast with investigations on **I** and **II**. Consistent with the relative Nd enhancement in the perovskite-based phase, an impurity with the cation ratio $CaBaFe_4$ was detected, which corresponds to the already-reported $CaBaFe_4O_8$ phase.[33] This phase has most certainly been reduced, given the reducing conditions of the last steps of the synthesis process. The diffraction pattern of this impurity then appears to be quite different from that of the O_8 stoichiometric reported phase, so that we could not add it to our structural refinements as a second phase.

Average structure refinement with neutron diffraction at ambient temperature is complicated by the need to accurately model the magnetic scattering ($T_N \approx 700$ K for **III**), and so refinement of SXRD data at room temperature was the first step.

---

(32) Oikawa, K.; Kamiyama, T.; Kanno, R.; Izumi, F.; Ikeda, T.; Chakoumakos, B. C. *Epdic 8: European Powder Diffraction*; Trans Tech Publications Ltd.: Zurich-Uetikon, 2004; Vol. 443-4, pp 337−340.

(33) Collins, D. M. *Nature* **1982**, *298*, 49–51.

This is followed by high-temperature neutron diffraction to resolve the distribution of the three cations over the available A sites, and finally combined refinement of high-Q ambient-temperature neutron data with SXRD data to extract maximum information concerning the Fe coordination environment.

Initial X-ray refinements were performed on data recorded on station 9.1 at SRS Daresbury in the *Imma* cell determined by ED. Initial atomic positions were obtained by reduction of symmetry based on a simple cubic perovskite supercell, yielding the starting atomic positions in Table S2 (Supporting Information). The heavy-atom positions were refined together with the occupancy of the A sites (treated in terms of Ba fractional occupancy at this stage). Anion vacancies were then located by MEM analysis after conventional Fourier synthesis methods had failed.

Several REMEDY cycles[24] were performed, and the fit improved from $R_{\mathrm{wp}} = 12.43$, $R_{\mathrm{e}} = 1.65$, $S = 7.52$, and $R_{\mathrm{I}} = 22.18$ to $R_{\mathrm{wp}} = 6.24$, $R_{\mathrm{e}} = 1.42$, $S = 4.40$, and $R_{\mathrm{I}} = 1.07$ after four cycles (Figure 4a,b). Inspection of the resultant MEM electron density maps using VEND[23] indicated that the O(2) and O(6) sites in the starting model are vacant (Figure 4c), producing a starting model for Rietveld refinement. Figure 5a shows that O(6) is at the level of Fe(3) in the Fe(3)O_2 layer, where the vacancies appear to generate a tetrahedral metal site, while O(2) is in the A(1)O rock-salt layer and produces square-based pyramidal co-ordination at neighboring Fe(1) sites. These anion vacancies thus produce three distinct A-site and three distinct B-site coordination environments, matching the distinct crystallographic sites available in *Imma* symmetry.

Final refinements were carried out using the GSAS refinement program and the Stephens model[34] to deal with the anisotropic strain broadening. There are three symmetry-inequivalent A sites in the structural model, and the initial refinement of the X-ray data involved assigning Ba to each site and then refining the fractional occupancies to 0.885(3), 0.867(2), and 0.720(2) on A sites 1, 2, and 3, respectively, indicating that *partial* cation ordering occurred between them, so that the composition of the three different sites was different. The X-ray scattering powers of Ba and Nd are very similar, so that it is not possible to define the true composition of the different A sites with X-ray data alone, requiring the analysis of the high-temperature neutron diffraction data described later, but other key structural features can be defined with the SXRD data. All oxygen positions were constrained to have the same displacement parameters, as were all the A sites. Oxygen site occupancies were allowed to refine (including those on positions corresponding to vacancies in the MEM maps), confirming that O(2) and O(6) were vacant and giving the Fe(3) layer a composition FeO. The positions of Fe(3) and O(7) in the tetrahedral Fe(3)O layer display disorder similar to that seen in the *ac* plane of the tetrahedral layer of the $3a_{\mathrm{p}}$ phase **II**, signaled by initial refinement of O(7) to a low occupancy. Refinement of Fe(3) and O(7) disordered onto half-occupied positions displaced from the mirror plane produced the final model (Figure 5a). Thus, there are three different coordination types corresponding to the three different Fe sites: Fe(3) is tetrahedral, Fe(2) octahedral, and Fe(1) square-based pyramidal. The refined oxygen content from the X-ray analysis is 15.6. Because the average Fe oxidation state expected was then less than 3, titrations were performed using the cerimetric method. The average titrated oxygen content found, 15.57(5), is in good agreement with the refined value.

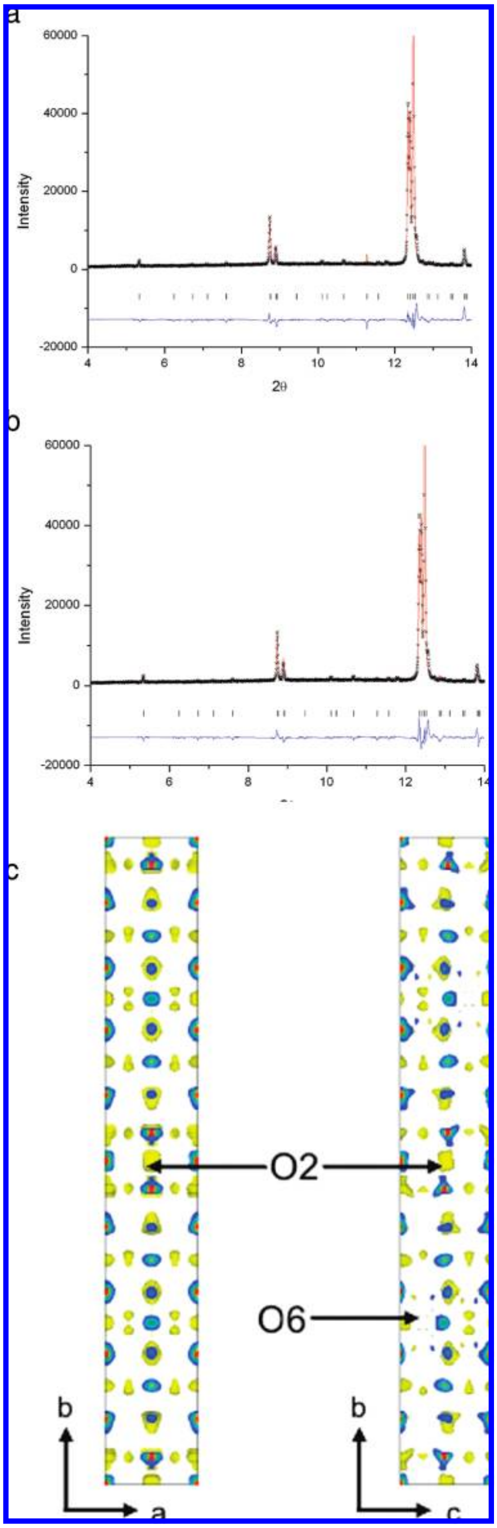

Figure 4. Comparison of the low-angle fit obtained to synchrotron X-ray data from **III** (a) before and (b) after the REMEDY cycles. Black crosses represent observed data, the red line the calculated intensity, green line difference, blue line background, and black vertical lines Bragg peak positions. (c) MEM electron density maps indicating vacancy locations in $Ca_2Ba_2Nd_2Fe_6O_{15+\delta}$. Yellow iso-surfaces are drawn at 10 electrons. (1 bohr = 0.529177211 Å: Bohr radius). Where atoms cut the cell edges, contours are drawn (from blue to red) in increments of 1 electron. The vacant sites are highlighted.

Variable-temperature powder neutron diffraction data (D20, ILL) showed that **III** exhibits magnetic reflections at room

---

(34) Collins, D. M. *Z. Natur. A* **1993**, *48*, 68–74.

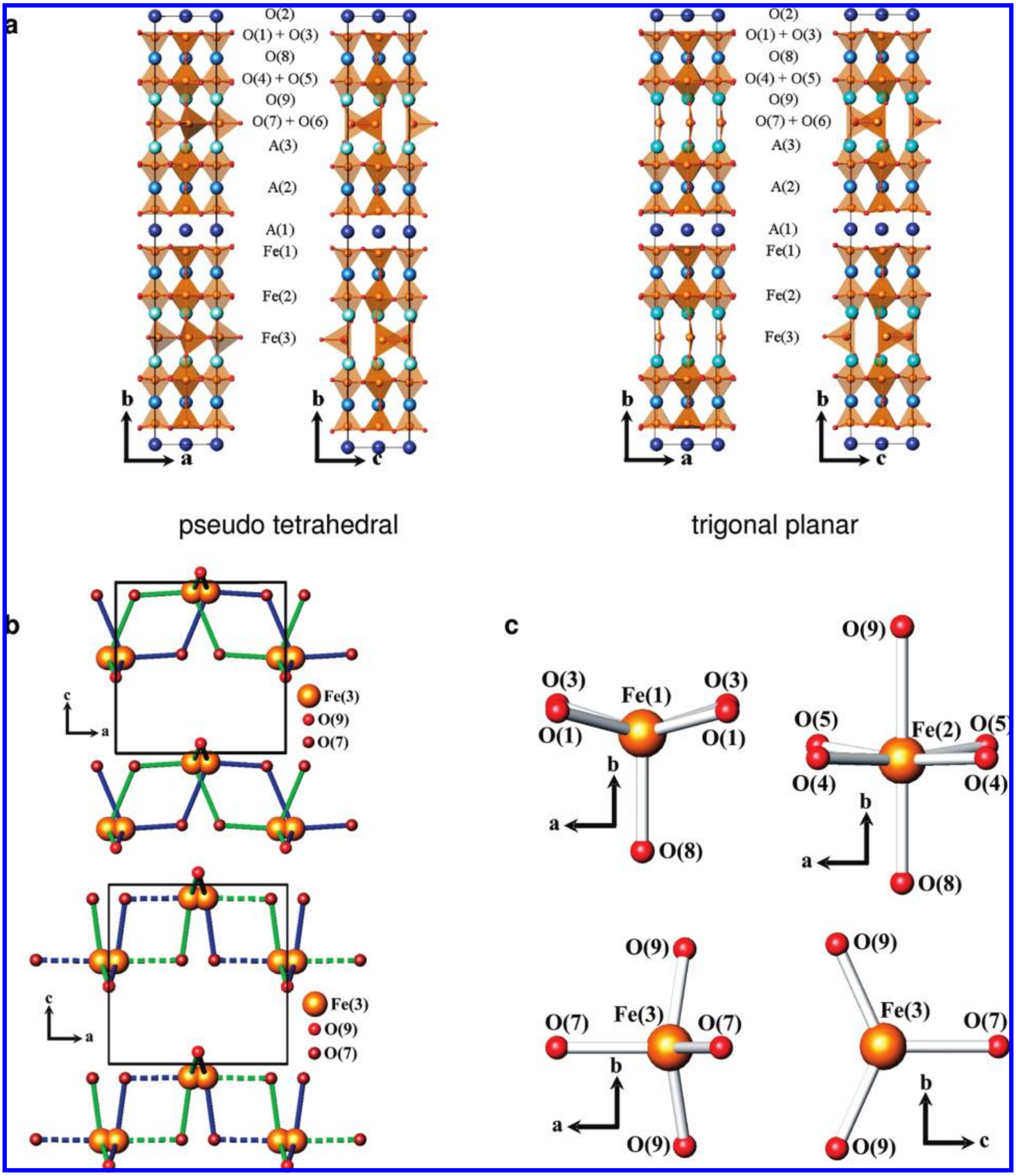

Figure 5. (a) View of the refined $Ca_2Ba_2Nd_2Fe_6O_{15.6}$ structure of **III** in *Imma*, showing the two alternative descriptions of Fe(3) connectivities; only one orientation of the Fe(3)−O_x polyhedron is shown for clarity. (b) View of the $Ca_2Ba_2Nd_2Fe_6O_{15.6}$ refined structure in *Imma*, showing the alternative disordered Fe(3)−O(7) connectivities in the *ac* plane as green and blue bonds. Both possible interpretations of the Fe(3) coordination are shown: tetrahedral (α, above) and trigonal (*β*, below). The two symmetry-related orientations are distinguished by bond color. (c) Iron coordination polyhedra in $Ca_2Ba_2Nd_2Fe_6O_{15.6}$ refined structure in *Imma* showing both alternative choice of Fe(3) connectivities.

temperature, but these reflections do not persist above 700 K (Figure S8, Supporting Information). Following these measurements, data suitable for structure refinement were then recorded at 773 K on the D2B diffractometer. The most notable difference in the oxygen positions at high temperature, in comparison with the X-ray refinement at room temperature, is the appearance of further disorder at the level of the Fe(3) environment at the tetrahedral site (Table S3a, Supporting Information). The equatorial O(6) site in the Fe(3)O layer is now partially occupied (24(7)%; however, the large thermal parameter could indicate a split site or lower occupancy and thus the O content is approximate), whereas the O(9) site linking Fe(2) and Fe(3) becomes less than fully occupied (0.81 on an 8h site). The onset of this disorder upon heating is consistent with orientational disordering of the tetrahedral chains around Fe(3), giving both orientations of tetrahedra (T′ and T), and with the oxygen

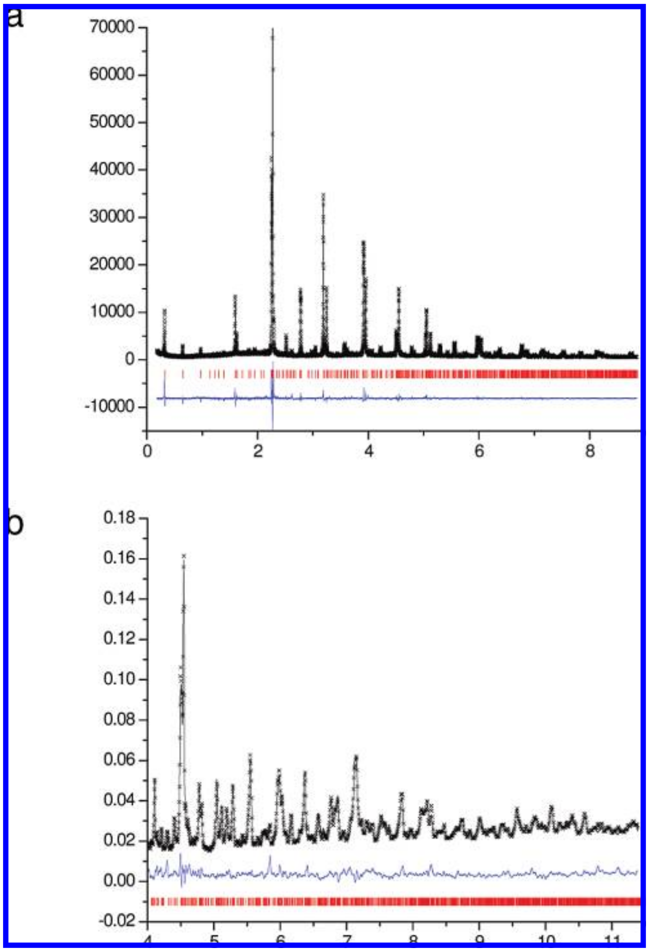

Figure 6. Rietveld refinement of (a) powder X-ray diffraction data and (b) high-Q neutron diffraction data from $Ca_2Ba_2Nd_2Fe_6O_{15.6}$ (**III**) at room temperature. Space group *Imma*; $a = 5.55997(3)$ Å, $b = 38.7062(2)$ Å, and $c = 5.58067(3)$ Å.

vacancies originally confined to the Fe(3)−O(7) layer becoming disordered into the neighboring AO layer, as in a high-temperature order−disorder transition in a brownmillerite.[30,31,35] A full description of the two orientations of the resulting tetrahedra (with the orientations of vacancies both within and out of the $Fe(3)O_{2-x}$ plane) would require more Fe(3) sites than can be stably refined from the data available. The refined O content remains the same within the error limits (15.44(18)) as that determined at room temperature from the XRD data. This high-temperature neutron diffraction model does not fit the room-temperature SXRD as well as the model refined against the room-temperature data, indicating that the oxygen site occupancy distribution in **III** changes upon heating.

The cation occupancy of the different A sites is given in Table 1. It is notable that no Ba is found on the A(1) site, which has the lowest oxide coordination number. This result is in good agreement with the fact that Ba is more likely to be situated on a high-coordination-number environment. This analysis, with the intrinsic assumption that the A sites are fully occupied, reveals that allowing the composition of the A sites to vary from the nominal cationic composition $Ca_2Ba_2Nd_2$ gives a refined composition of $Ca_{1.9}Ba_{1.9}Nd_{2.2}Fe_6$, in agreement with the EDS results and with the observation of an impurity phase which contains Ba and Ca but not Nd. Considering a 15.6 oxygen content, this formulation leads to a 2.83+ average oxidation state for Fe in **III**. Following this analysis of the composition, we then re-introduced the calculated A-site compositions back into both the room-temperature X-ray and the high-temperature neutron refinements. No degradation of the fit was observed compared to the approximate two-cation-site composition model used in the initial refinements of both individual data sets, validating the procedure adopted. The final reliability factors obtained are then $R_{wp} = 7.41\%$, $R_p = 6.26\%$, $R(F^2) = 3.75\%$, and $\chi^2 = 2.35$ for the X-ray refinement and $R_{wp} = 5.39\%$, $R_p = 3.82\%$, $R(F^2) = 9.47\%$, and $\chi^2 = 10.43$ for the neutron refinement.

Once the A-site distribution was determined, joint refinements of the synchrotron and high-Q (defined as the range where no magnetic scattering was observed, estimated from the room-temperature D20 data) regions of the ambient-temperature GEM data obtained for the first sample of phase **III** were carried out, as both data sets correspond to the same sample. The neutron data are comparatively insensitive to A-site order but more sensitive to displacements of the oxide anions, as the X-ray-only refinement is likely to be less sensitive to the details of the Fe(3)−O(7) order. In the refinements, the A-site cation distribution was fixed as above, and the remaining positions and isotropic thermal parameters were refined. Refinement in *Imma* yielded convergence to $\chi^2 = 6.90$ for 102 variables. The

Table 1. Refined Coordinates of $Ca_2Ba_2Nd_2Fe_6O_{15.6}$ (**III**) from the Combined Refinement[a]

atom	multiplicity	occupancy	*x*	*y*	*z*	$U_{iso} \times 100$ (Å^{-2})
Fe(1)	8h	1.0	0	0.04965(4)	0.5098(4)	0.0032(2)
Fe(2)	8h	1.0	0	0.15191(5)	0.4999(4)	0.0020(2)
Fe(3)	8i	0.5	0.0435(8)	$^1/_4$	0.5723(6)	0.0129(8)
O(1)	8g	1.0	$^1/_4$	0.04292(9)	$^1/_4$	0.0136(6)
O(3)	8g	1.0	$^1/_4$	0.96249(8)	$^1/_4$	0.0046(5)
O(4)	8g	1.0	$^1/_4$	0.15272(8)	$^1/_4$	0.0014(4)
O(5)	8g	1.0	$^1/_4$	0.65752(8)	$^1/_4$	0.0102(5)
O(7)	8i	0.5	0.4085(16)	$^1/_4$	0.5794(15)	0.0096(13)
O(8)	8h	1.0	0	0.10009(9)	0.5251(7)	0.0117(5)
O(9)	8h	1.0	0	0.2057(1)	0.4328(13)	0.0506(19)
Nd(1)	4a	0.743	0	0	0	0.0033(3)
Ca(1)	4a	0.257	0	0	0	0.0033(3)
Nd(2)	8h	0.37	0	0.59925(5)	−0.0084(6)	0.0134(3)
Ba(2)	8h	0.406	0	0.59925(5)	−0.0084(6)	0.0134(3)
Ca(2)	8h	0.224	0	0.59925(5)	−0.0084(6)	0.0134(3)
Nd(3)	8h	0.167	0	0.69341(4)	−0.0184(5)	0.0070(3)
Ba(3)	8h	0.405	0	0.69341(4)	−0.0184(5)	0.0070(3)
Ca(3)	8h	0.427	0	0.69341(4)	−0.0184(5)	0.0070(3)

[a] Space group *Imma*; $a = 5.55997(3)$ Å, $b = 38.7062(2)$ Å, and $c = 5.58067(3)$ Å.

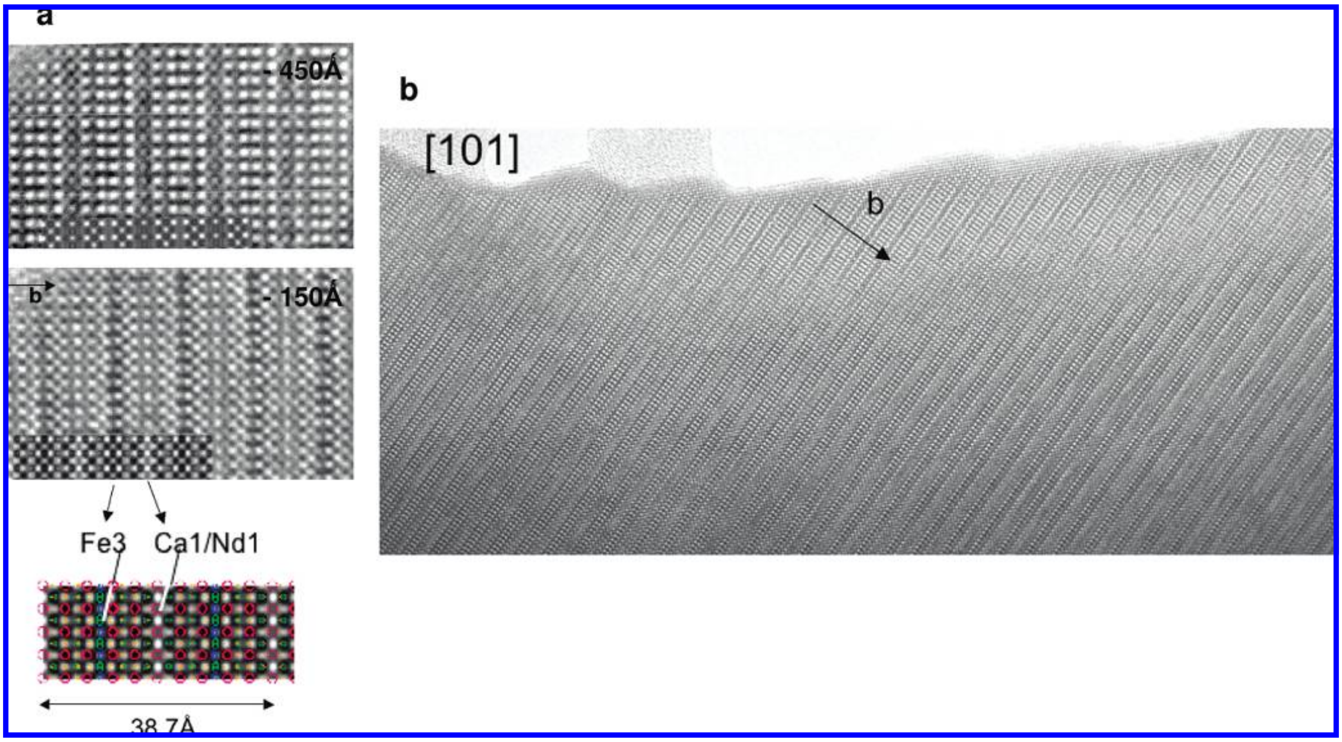

Figure 7. (a) HRTEM images of the $10a_p$ phase **III**. Two enlarged [101] images, with the superposed simulated ones, are shown, recorded for focus values close to −450 and −150 Å, respectively. (b) Enlarged image of **III** showing a defect-free region of the structure. Two of the blocks along *b* correspond to the 38 Å repeat.

refined coordinates are given in Table 1, and views of the structure are given in Figure 5. The Rietveld fit to the X-ray and neutron data is shown in Figure 6.

HRTEM images (Figure 7a) indicated that the $10a_p$ structure of the material corresponded to an ordered intergrowth of distinct bilayer and trilayer sequences of B-site cations, consistent with the structure refined from neutron and X-ray data. The enlarged projected potential calculated from the refined coordinates and occupancies in Table S1 and the atom overlay allow the main contrast to be associated with the $10a_p$ structure: as an example, for a focus value of 150 Å, the brighter dots are associated with the low-electron-density zones, so that the darker row corresponds to the [Fe(3)−O7] layer, whereas the brighter dots are due to the oxygen vacancies between the Ca1/Nd1 positions. The HREM analyses of numerous crystals show that the stacking mode of the layers is regular throughout the material. This is illustrated by an overall view of a crystal (Figure 7b) exhibiting zero defects.

Table 2a shows the Fe−O distances around the three different Fe sites (Figure 5c). Fe(1) has a square-based pyramid environment with four similar distances within the square plane and a slightly shorter apical Fe(1)−O(8) distance. This is similar to the square-pyramidal site found in $YBa_2Fe_3O_8$,[32] where the basal plane distances are 2.02 Å and the apical distance is 1.8405 Å. The bond valence sum (BVS) at the Fe(1) site is 2.64+. Fe(2)-has an octahedral environment with four close equatorial Fe−O distances of slightly less than 2 Å. The Fe(2)−O(8) apical bond is close to these values, whereas the octahedron is elongated along the O(9) direction (2.11769(2) Å) due to the short Fe−O distances at the low-coordinate Fe(3) site. In $YBa_2Fe_3O_8$, the octahedral environment is also strongly distorted, with four 1.959 Å contacts and two axial 2.18 Å distances. The distorted octahedral Fe(2) has a BVS of 3.11+. The long Fe(2)−O(9) contact produces a short Fe(3)−O(9) axial contact, which distorts the environment of Fe(3) significantly relative to the regular tetrahedral environments in **II**, which have 1.93 Å as opposed to 1.89 Å contacts to the two oxygen neighbors which lie out of the FeO plane.

Analysis of the geometry around Fe(3) is more difficult, as the refined environment is unusual. There are two Fe(3)−O(9) distances of 1.89683(2) Å. The Fe(3)−O(7) plane is positionally disordered, with both Fe(3) and O(7) displaced from higher symmetry sites and half-occupied. Two possible iron−oxygen environments can be constructed from these disordered sites. The first possibility (labeled α in Table 2a) has Fe(3) in a pseudo-tetrahedral environment with two almost equal equatorial Fe(3)−O(7) distances (2.03034(2) and (2.08413(2) Å, Figure 5a,b, left, and Figure 5c, bottom left). The Fe(3) BVS is 2.27 for this site, and it should be noted the coordination environment is highly non-symmetrical, with O(7)−Fe(3)−O(9) angles (Table 2b) deviating significantly from the tetrahedral (at ∼115 and ∼97° for the closest contacts; see CIF files in Supporting Information). Alternatively, we can consider Fe(3) to be trigonal planar (β) with one short (1.96264(2) Å) and one very long (2.51352(3) Å) Fe(3)−O(7) contact (Figures 5a,b, right, and Figure 5c, bottom right). The Fe(3) BVS is 1.95 for this arrangement.

The *Imma* symmetry corresponds to disorder in the Fe(3)−O(7) layer. The alternative space group *I2mb* is also consistent with the systematic absences shown in the ED and permits ordering of O(7) to give either the tetrahedral α or the trigonal β Fe(3) coordination. Refinement of the two competing ordered structures in *I2mb* (Figure 5b) did yield slightly improved fits: $\chi^2 = 6.70$ for 116 variables for a model based on pseudo-tetrahedral Fe(3) (α) and $\chi^2 = 6.58$ for 116 variables for a model with three-coordinate Fe(3) (β) (CIF files for the latter refinement

---

(35) Stephens, P. W. *J. Appl. Crystallogr.* **1999**, *32*, 281–289.

Table 2. (a) Fe−O Distances around the Different Fe Sites, (b) O−Fe−O Angles around the Different Fe Sites and Bridging Fe−O−Fe Angles, and (c) A−O Distances at the Different A Sites from the Combined Refinement of **III** at Room Temperature in *Imma*

(a) Fe−O Distances

	distance (Å)	*n*	occupancy of the O site
Fe(1)−O(1)	2.02575(1)	×2	1
Fe(1)−O(3)	1.98744(1)	×2	1
Fe(1)−O(8)	1.95449(2)	×1	1
Fe(2)−O(4)	1.96936(1)	×2	1
Fe(2)−O(5)	1.98210(1)	×2	1
Fe(2)−O(8)	2.01057(1)	×1	1
Fe(2)−O(9)	2.11769(2)	×1	1
Fe(3)−O(9)	1.89683(2)	×2 (α,*β*)	1
Fe(3)−O(7)	2.03034(2)	1(α)	½
Fe(3)−O(7)	2.51352(3)	1(*β*)	½
Fe(3)−O(7)	1.96264(2)	1(*β*)	½
Fe(3)−O(7)	2.08413(2)	1(α)	½

(b) O−Fe−O Angles

	angle (°)		angle (°)
O(1)−Fe(1)−O(1)	86.67(8)	O(1)−Fe(1)−O(2)	2 × 81.45(10)
O(1)−Fe(1)−O(3)	2 × 158.82(13)	O(1)−Fe(1)−O(3)	88.424(25)
O(1)−Fe(1)−O(8)	99.17(12)	O(1)−Fe(1)−O(3)	88.424(25)
O(1)−Fe(1)−O(8)	99.17(12)	O(2)−Fe(1)−O(3)	77.45(9)
O(2)−Fe(1)−O(3)	77.45(9)	O(3)−Fe(1)−O(3)	88.76(8)
O(3)−Fe(1)−O(8)	2 × 101.95(12)		
O(4)−Fe(2)−O(4)	89.81(8)	O(4)−Fe(2)−O(5)	2 × 172.79(14)
O(4)−Fe(2)−O(5)	2 × 90.111(10)	O(4)−Fe(2)−O(8)	2 × 93.77(12)
O(4)−Fe(2)−O(9)	2 × 81.90(16)	O(5)−Fe(2)−O(5)	89.07(8)
O(5)−Fe(2)−O(8)	2 × 93.43(12)	O(5)−Fe(2)−O(9)	2 × 90.95(16)
O(5)−Fe(2)−O(8)	93.43(12)	O(5)−Fe(2)−O(9)	90.95(16)
O(8)−Fe(2)−O9	173.85(23)		
O(7)*β*−Fe(3)−O(7)α	81.04(34)	O(7)α−Fe(3)−O(7)α	109.96(30)
O(7)α−Fe(3)−O(9)	2 × 97.79(16)	O(7)α−Fe(3)−O(7)*β*	28.9(4)
O(7)*β*−Fe(3)−O(9)	2 × 115.05(21)	O(7)α−Fe(3)−O(9)	2 × 109.66(21)
O(9)−Fe(3)−O(9)	129.2(4)		
Fe(2)−O(4)−Fe(2)	178.1(2)	Fe(1)−O(1)−Fe(1)	165.2(2)
Fe(2)−O(5)−Fe(2)	167.4(2)	Fe(1)−O(3)−Fe(1)	152.6(2)
Fe(2)−O(8)−Fe(1)	173.5(2)	Fe(3)−O(7)−α-Fe(3)	112.2(4)
Fe(2)−O(9)−Fe(3)	144.8(4)	Fe(3)−O(7)−*β*-Fe(3)	98.9(3)

(c) A−O Distances

	distance (Å)	*n*	occupancy of the O site
A(1)−O(1)	2.5773(23)	×4	1
A(1)−O(3)	2.4470(19)	×4	1
A(2)−O(1)	2.9162(35)	×2	1
A(2)−O(3)	3.118(3)	×2	1
A(2)−O(4)	2.8350(31)	×2	1
A(2)−O(5)	3.0160(34)	×2	1
A(2)−O(8)	2.7867(4)	×2	1
A(2)−O(8)	2.884(5)	1	1
A(2)−O(8)	2.698(5)	1	1
A(3)−O(4)	2.467(3)	2	1
A(3)−O(5)	2.472(3)	2	1
A(3)−O(3)	2.314(3)	2	½
A(3)−O(9)	2.834(1)	2	1
A(3)−O(9)	2.362(8)	2	1
A(3)−O(9)	3.302(8)	1	1

can be found in the Supporting Information). Given the number of extra parameters in *I*2*mb* and the relatively small change in χ^2, the structure will be discussed in terms of the *Imma* structure, though these refinements appear to support the trigonal coordination environment β for Fe(3). It should also be noted that, while Fe(II) seldom forms tetrahedra in oxides, there are more examples of trigonal planar systems with this oxidation state,[36–39] which is favored over tetrahedral coordination for d^6 ions on ligand field stabilization energy (LFSE) grounds.[40,41] It is interesting to note that three-coordinate environments are found for Fe^{2+} in highly reduced $n = 3$Ruddlesden−Popper phases.[39] The trigonal geometry is a compressed?xpp foot;6894ref36;10?> Y shape according to the bond angles.

The connectivity between the different iron polyhedra is controlled by the bridging oxygen angles given in Table 2b, which are in the expected ranges given the average A cation sizes. The distorted bridging angle between the octahedral Fe(2) and tetrahedral/trigonal Fe(3) sites is similar to the 141.8° angle

---

(36) Berastegui, P.; Hull, S.; Garcia-Garcia, F. J.; Eriksson, S. G. *J. Solid State Chem.* **2002**, *164*, 119–130.

(37) Amann, P.; Moller, A. *Z. Anorg. Allg. Chem.* **2002**, *628*, 917–919.

(38) Cuevas, J. V.; Palacios, A. A.; Alvarez, S. *New J. Chem.* **1997**, *21*, 301–308.

(39) Moller, A. *Z. Kristallogr.* **1996**, *211*, 325–325.

(40) Bowman, A.; Allix, M.; Pelloquin, D.; Rosseinsky, M. J. *J. Am. Chem. Soc.* **2006**, *128*, 12606–12607.

(41) Alvarez, S. *Coord. Chem. Rev.* **1999**, *195*, 13–41.

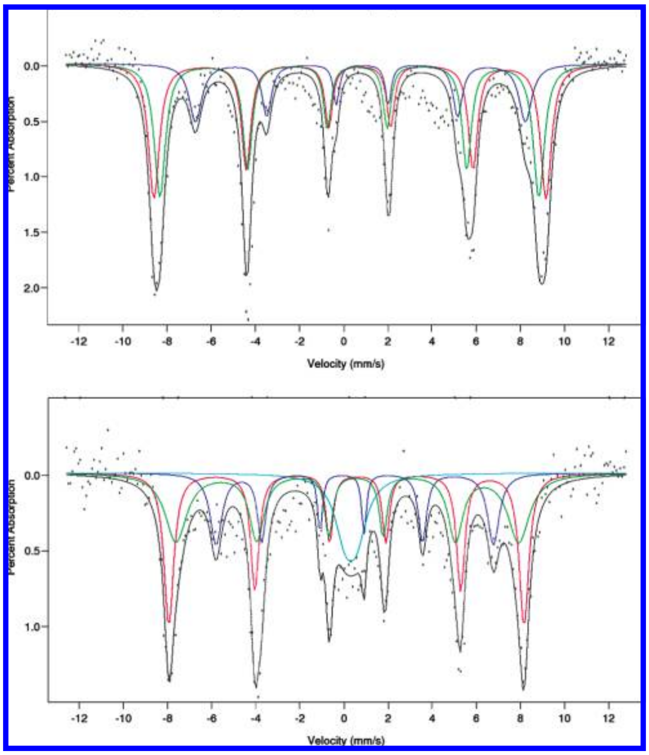

Figure 8. Mössbauer spectra of $Ca_2Ba_2Nd_2Fe_6O_{15.6}$ (**III**) reported at 77 K (a) and room temperature (b). The fitted parameters for the three crystallographically distinct iron sites are reported in Table S6 (Supporting Information).

subtended at the oxide bridging octahedra and tetrahedra in the brownmillerite $Sr_2Al_{1.07}Mn_{0.93}O_5$,[29] supporting the chemical reliability of the model derived here.

The variable-temperature neutron data indicate that **III** is magnetically ordered below 773 K. Mössbauer measurements on **III** at 77 K revealed multiple sets of six line patterns, consistent with the entire sample being magnetically ordered. The spectrum can be fitted using three different Fe sites, consistent with the crystal structure model. The complexity of the global pattern resulting from the contribution of three sets of six line patterns required the fitting parameters to be constrained. Thus, the integrated areas have been constrained to match a 2:2:1 ratio in agreement with the structural model (Fe(1), 2; Fe(2), 2; Fe(3), 1). The fitted patterns are shown in Figure 8a, and the characteristic values of the fit at 77 K are given in Table S5 (Supporting Information). The Fe site corresponding to the smallest area, i.e., Fe(3), has a chemical shift higher than the other sites and a lower hyperfine field, consistent with Fe^{2+}.[42] Considering the Fe(3) to be 2+, this leads us to a 3+ oxidation state for the Fe(1) and Fe(2) sites from the chemically determined overall oxidation state distribution. The chemical shift of these sites is within the expected values for this oxidation state. Octahedral Fe^{3+} in $Ca_2Fe_2O_5$ occurs at 0.46 mm s^{-1} with a negative quadrupolar splitting, close to the isomer shifts for both other resonances observed in $YBa_2Fe_3O_8$, similar shifts are observed for Fe^{3+} in both square-planar and octahedral (elongated) environments. In $SmBaFeO_{5.25}$, with a mean iron oxidation state similar to that of **III**, the 5- and 6-coordinate iron resonances occur at almost equal isomer shifts.[16] Resonances A and B are thus assignable to the octahedral and square-based pyramidal sites, with oxidation states consistent with the observed environments. BVS analysis partitions the mean 3+ charge on these two sites as an excess (3.11+) on the octahedral Fe(2) site and an enhanced Fe^{2+} content (2.65+) on square-based pyramidal Fe(1). The assignment of Fe^{2+} to the Fe(3) site is consistent with the overall mean Fe 2.83+ oxidation state derived from the refined A-site cation distribution.

The temperature dependence of the magnetic susceptibility of **III** is shown in Figure S9a (Supporting Information). The room-temperature Mössbauer pattern (Figure 8b) shows that the magnetic ordering is incomplete due to the broad, non-magnetic feature appearing in the middle of the spectrum. Neutron data show that there is long-range magnetic order up to 773 K, consistent with a magnetic transition taking place between 77 and 300 K, involving ordering of the remaining spins within the sample. There is a pronounced irreversibility between the zero-field-cooled and field-cooled data (500 Oe), indicative of a magnetic transition at 250 K. Figure S9b shows magnetization versus field at two different temperatures. Hysteresis is observed at 77 K but cannot be assigned to bulk ferromagnetism because of the small magnetization measured (0.09 μ_B per Fe site). A canted antiferromagnetic or spin-glass-like state is indicated.

Defects within III. Given the complexity of the refined structure and the existence of a range of defects (Figure 2d) in the $3a_p$ structure **II**, defects are to be expected in **III**. The study of a large number of crystals does allow the detection of three main structural mechanisms for defect formation.

Defective Members. In the matrix of phase **III**, a few defective members have been detected, which allow understanding of the range of structures which may subsequently be accessible by the modular approach. They mainly consist of the formation of small domains of the $3a_p$ phase in the $10a_p$ matrix. One example is given in Figure 9a, where the defect is observed in the right part of the $[10\bar{1}]$ HREM image. The domain boundary is perfectly coherent, as the two phases exhibit parallel *b* axes (with periodicities of $3a_p$ and $10a_p$, respectively) and common perpendicular polyhedral layers. The octahedral Fe(2) site in **III** links the two phases together through its coordination to tetrahedral Fe(3) (bridging to **II**) and square-pyramidal Fe(1). The situation is different when the two phases grow perpendicularly, since different distorted iron polyhedra have to be accommodated through the boundary. This is shown by the [001] image in Figure 9b, where the misfit clearly appears as one polyhedral layer becomes common every $15a_p$. The $10a_p$ phase is observed in the upper part of the image and the $3a_p$ in the bottom. The average boundary is roughly horizontal, shown by a dotted line but actually corresponding to a zone of striped contrast of a few tens of nanometers width, across which the iron polyhedra are rearranged. The image shows that the structural transition mechanism operates over a $15a_p$ distance. A third defective member is shown in Figure 9c. For this focus value, close to the Scherzer value (i.e., −300 Å for the electron microscope), and a thickness estimated close to 28 Å, the contrast of the [001] image consists mainly of the regular alternation of two rows of brighter spots, separated by three rows of less bright dots (see the calculated image superposed on the experimental image in the thin part of the crystal). All these rows are associated with the rows of Nd/Ca cations, the two brighter ones being those sandwiching the Fe(3) atoms. This "2−3" regular contrast is associated with *b*/2, i.e., half of the periodicity of the $10a_p$ structure. The defective members

---

(42) Cirera, J.; Alemany, P.; Alvarez, S. *Chem.-Eur. J.* **2004**, *10*, 190–207.

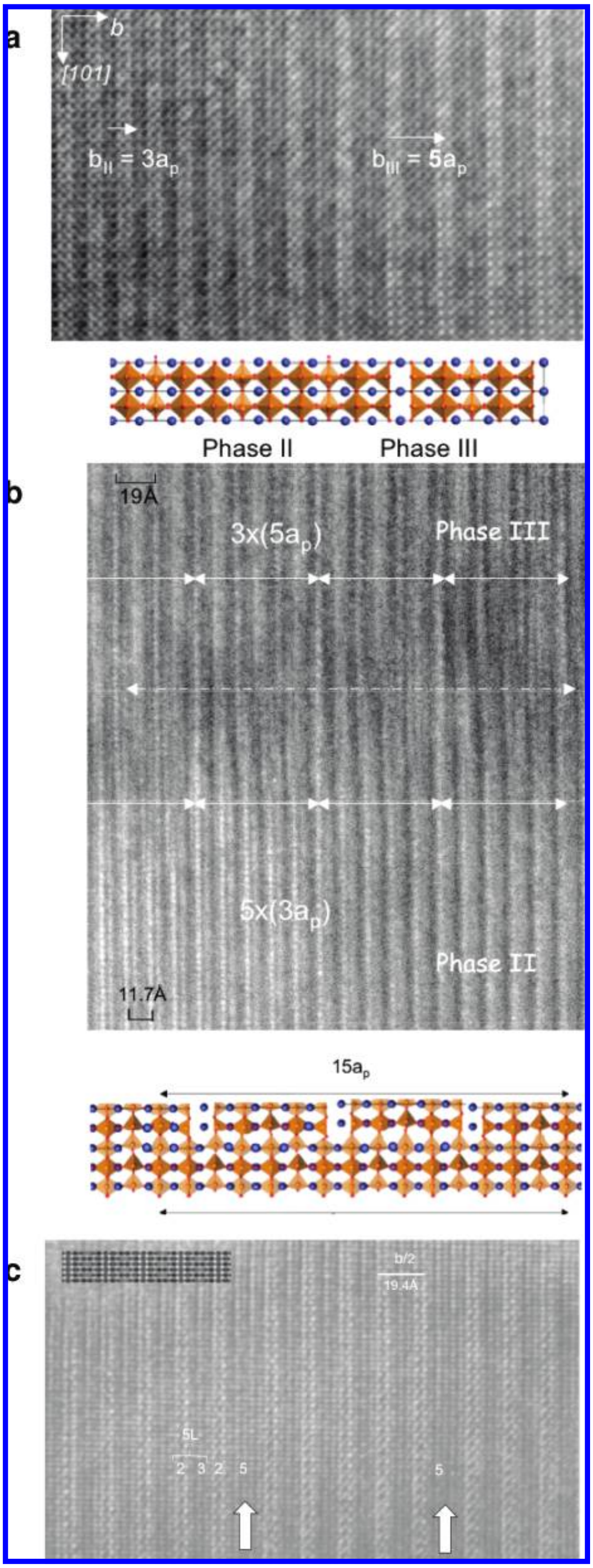

Figure 9. Defects within the 10-layer structure of **III**. (a) Coherent intergrowth with $3a_p$ phase **II** along *b*. (b) Accommodation of perpendicular domains of **I** and **III**. (c) The white arrows mark the insertion of two extra layers into the three-layer component of the five-layer structure to give a local formation of a seven-layer block.

correspond to the appearance of two extra layers in a 2−3 regular matrix and involve the local formation of 2−5 defective members.

Local Variation of the Contrast. Point-like variations of the contrast are locally observed. Most of them are associated with local variation of the oxygen content, and they are particularly found in the Fe(3)−O(7) layer, which is consistent with the results of the refinement, but also in other layers of the structure. One example is given in Figure S10 (Supporting Information), with the alternation of one bright and one less bright spot, giving a local periodicity of $2d_{101} \approx 2a_p$.

Twinning Domains. The very weak and rather diffuse streaks observed in the [001] ED pattern (Figure 3c,d) are partly generated by the existence of twinning domains, resulting from the particular relationships between the cell parameters of the $10a_p$ phase, namely $a \approx c$ due to the orthorhombic distortion of a pseudo-tetragonal structure on the one hand and $a\sqrt{2} \approx c\sqrt{2} \approx b/5$ on the other hand. One example of the latter arrangement of two variants is given in Figure S11 (Supporting Information), where two 90°-oriented [101] domains exhibit a non-coherent twin boundary.

Discussion

Electron and synchrotron X-ray diffraction on the cubic air-synthesized precursors **I** at the 2:1 ratio of precursor units and analogues at the 1:1 and 1:2 ratios shows the correlation between A-site compositional diversity and anion composition and vacancy ordering in the Nd−Ba−Ca−Fe oxide system. The cubic systems all have Fe oxidation states higher than 3+. The cubic systems **I** show diffuse ED features, consistent with short-range order of either or both oxygen vacancies and A-site cations.

In the Fe^{3+} compound $Ca_2Nd_2Ba_2Fe_6O_{16}$ (**II**), the B cations in the system occupy octahedral and tetrahedral sites as in the parent compound $Sr_2LaFe_3O_8$. The anion vacancy ordering also creates two distinct A cation sites, and here the availability of three different sizes and charges of cations produces cation ordering on the A site as well. The X-ray refinements are consistent with the barium cation preferentially occupying the larger A site at the center of the octahedral layers. Displacement of both iron and oxygen in the vacancy containing an FeO layer produces orientational disorder of approximately regular tetrahedra, consistent with the Fe^{3+} oxidation state.

Further reduction of the Fe oxidation state from 3+ in **II** affords the 10-layer phase **III**. The temperature at which oxygen is removed is sufficiently high to permit cation rearrangement to match the A- and B-site geometry to the overall oxygen content. In the context of the failure to repeat the initial gas-flow reactions which led to the identification of the 10-layer phase, it should be noted that the precursor to treatment with the appropriate pO_2 is itself important. Thus, the cubic material from the 1200 °C reaction, with its variable modes and domain sizes of ordering, is not a reliable precursor—the $3a_p$ phase **II** itself has not only well-defined anion vacancy but also cation site ordering and is thus a much more suitable precursor, especially as the reactions to afford the $10a_p$ phase necessarily take place at *T* lower than 1200 °C, making cation rearrangement by diffusion more difficult. The initial reaction is intrinsically hard to reproduce because the O_2 partial pressure in the flow generated by the Fe gettering itself depends on the state of oxidation of the Fe and the initial N_2 purity. Even with very fine control of the pO_2 (which had the advantage of yielding the 3-layer phases discussed below), direct reaction does not afford the $10a_p$ phase, and thus the two-step sealed-tube controlled O content route is required.

A-site ordering in perovskite-based structures is unusual unless accompanied by anion vacancies to generate different coordination number sites. There are examples of A-site order in high-pressure-synthesized $NdAgTi_2O_6$ and $NaLaMgWO_6$, where layered A cation order is coupled with rock salt B-site order.[43,44] Considering the perovskite ABO_3 structure as a stacking of (AO) and (BO_2) layers, vacancies can occur in either of these components. Vacancies along the $(100)_p$ direction within the BO_2 layer generate square-pyramidal coordination, as found in $Ca_2Mn_2O_5$,[45] or alternating square-planar and octahedral coordination, as in $La_2Ni_2O_5$,[46] depending on whether vacancies are regularly distributed or alternate as no or two neighboring vacancy chains. Reduced vacancy concentration occurs in the three-dimensionally connected cuprate $BaLa_4Cu_5O_{14-x}$,[47] which has both square-pyramidal and octahedral metal coordination. The $La_{8-x}Sr_xCu_8O_{20}$[48] structure contains square-pyramidal coordination at the majority of copper sites, but combination of B-site environments with no missing anion rows (octahedral) and two missing neighboring rows (square-planar) gives the unusual combination of three different cation coordination environments in the same structure.[49]

Chains of vacancies along the $(110)_p$ direction within the BO_2 layer generate tetrahedral coordination at the metal sites, as in the brownmillerite structure of $Ca_2Fe_2O_5$. The alternation of BO_2 and BO layers generates alternate layers of octahedral and tetrahedral metal coordination. This structure affords a complex set of homologous series in which the spatial relationship of these layers is controlled: $Sr_2LaFe_3O_8$[50] and $Ca_4Fe_2Ti_2O_{11}$[51] have one and two extra octahedral layers, respectively, compared with $Ca_2Fe_2O_5$,[18] and $Ca_4YFe_5O_{13}$ is an ordered intergrowth of OTOT $Ca_2Fe_2O_5$ type and OOT $Sr_2LaFe_3O_8$ types.[52,53]

There is a wide variety of structures based on vacancies in the AO rock salt layers which generate square-pyramidal B cation environments. The alternation of AO and A layers generates the $YBaCuFeO_5$[54] structure with only square-pyramidal iron environments, as in the mixed-valence system $YBaFe_2O_5$. $LaBaMn_2O_5$[14] adopts this structure and is a route to $LaBaMn_2O_6$ with A-site order in the absence of oxygen vacancies. An ordered array of vacancies in an $AO_{0.5}$ layer gives the structure $Ba_2Y_2Mn_4O_{11}$,[55] in which there is a checkerboard ordering of octahedral and square-planar coordination environments. As in the BO_2 layer vacancy-based structures, more complex ordering of the vacancy containing layers gives rise to complex families of structures: $YBa_2Fe_3O_8$[32] features two AO and one A layer to generate two square-pyramidal iron sites flanking a central octahedral site, and $Ba_2La_2Cu_2Sn_2O_{11}$[56] inserts a second octahedral site into this sequence—these materials have the same formal composition as the $Sr_2LaFe_3O_8$ and $Ca_4Fe_2Ti_2O_{11}$ BO_2 vacancy-based materials. Combination of both layer vacancy types is seen in $LnSr_2Cu_2GaO_7$,[57] which has square-pyramidal copper due to AO layer vacancies and tetrahedral gallium due to $(110)_p$ chains of vacancies in the BO_2 layer.

The present 10-layer material **III** is unusual in that it features three crystallographically distinct environments for both A- and B-site ions within the perovskite-derived structure. Analysis of the Inorganic Crystal Structure Database, searching for materials with distinct environments at this level, did not reveal analogous structures. The 10-layer structure of **III** formally results from ordered intergrowth of the $YBaFe_2O_5$ structure type with square-pyramidal iron environments and the $Ca_2Fe_2O_5$ structure with tetrahedral and octahedral iron. Control of the oxygen content allows this structure to emerge from the three-layer $Nd_2Ca_2Ba_2Fe_6O_{16}$ with solely octahedral and tetrahedral iron environments. The Fe(3) site is distorted away from tetrahedral toward trigonal planar, consistent with Fe^{2+} occupancy of this site producing a difference in the FeO layer in the $10a_p$ structure compared with the $3a_p$ structure. The octahedral Fe(2) site has a higher 3+ content according to the average bond lengths than the square-based pyramidal Fe(1), which may be associated with the non-zero LFSE of d^6 Fe^{2+}. The mean charge state on the two Fe sites in the $Ca_2Fe_2O_5$ component of the structure is also lower than 3+ due to the unusual distorted geometry of Fe(3), showing that the actual charge distribution in **III** does not match that expected from the modular $Ca_2Fe_2O_5$ plus $NdBaFe_2O_5$ model, as the tetrahedral site distortion at Fe(3) produces a lower B-site charge in **III** than in $Ca_2Fe_2O_5$.

The 8-coordinate A1 site contains no barium, consistent with the idea that the large barium cation requires a higher coordination number. In $YBaFe_2O_5$ itself, this site is purely occupied by Y^{3+}. The distribution of cations over the other two available sites reflects the total exclusion of Ba from the 8-coordinate site and the availability of two sites with coordination numbers (10 and 12) that are acceptable for Ba. The calcium cation is located predominantly on the 8- and 10-coordinate sites and is at its lowest concentration on the 12-coordinate A(2) site between the octahedral and square-pyramidal sites at the interface between the brownmillerite BO_2 vacancy and AO vacancy layers.

The selection of A cations to generate multiple A sites gives access to new perovskite superstructures where the distribution of anion vacancies is controlled to optimize the A-site coordination. This could give access to systems tailored to optimize anion mobility, building on the example of $PrBaCo_2O_{5+x}$,[12,13] as well as offering distinct sites to a range of cations to enable new property combinations. The range of extended defects observed within **III** suggests that further superstructures based on ordered assembly of established A- and B-site order patterns will be accessible by control of O content and cation geometry

---

(43) Menil, F. *J. Phys. Chem. Solids* **1985**, *46*, 763–789.
(44) Knapp, M. C.; Woodward, P. M. *J. Solid State Chem.* **2006**, *179*, 1076–1085.
(45) Park, J. H.; Woodward, P. M.; Parise, J. B. *Chem. Mater.* **1998**, *10*, 3092–3100.
(46) Poeppelmeier, K. R.; Leonowicz, M. E.; Longo, J. M. *J. Solid State Chem.* **1982**, *44*, 89.
(47) Rao, C. N. R.; Gopalkrishnan, J.; Vidyasagar, K.; Ganguli, A. K.; Ramanan, A.; Ganapathi, L. *J. Mater. Res.* **1986**, *1*, 280.
(48) Michel, C.; Rakho, L. E.; Hervieu, M.; Pannetier, J.; Raveau, B. *J. Solid State Chem.* **1987**, *68*, 143.
(49) Aasland, S.; Fjellvag, H.; Hauback, B. C. *J. Solid State Chem.* **1998**, *135*, 103–110.
(50) Er-Rakho, L.; Michel, C.; Raveau, B. *J. Solid State Chem.* **1988**, *73*, 514.
(51) Gonzalez-Calbet, J. M.; Vallet-Regi, M. *J. Solid State Chem.* **1987**, *68*, 266.
(52) Bando, Y.; Sekikawa, Y.; Yamamura, H.; Matsui, Y. *Acta Crystallogr. A* **1981**, *37*, 723–728.
(53) Bando, Y.; Yamamura, H.; Sekikawa, Y. *J. Less Common Metals* **1980**, *70*, 281–284.
(54) Er-Rakho, L.; Michel, C.; LaCorre, P.; Raveau, B. *J. Solid State Chem.* **1988**, *73*, 531.
(55) Karppinen, M.; Okamoto, H.; Fjellvag, H.; Motohashi, T.; Yamauchi, H. *J. Solid State Chem.* **2004**, *177*, 2122–2128.
(56) Anderson, M. T.; Poeppelmeier, K. R.; Zhang, J.-P.; Fan, H.-J.; Marks, L. D. *Chem. Mater.* **1992**, *4*, 1305.
(57) Vaughey, J. T.; Thiel, J. P.; Groenke, D. A.; Stern, C. L.; Poeppelmeier, K. R.; Dabrowski, B.; Hinks, D. G.; Mitchell, A. W. *Chem. Mater.* **1991**, *3*, 935.

preference, particularly as the premonitory assembly of such superstructures occurs within the pseudo-cubic precursor **I** (Figure 2d).

The concept of modular structures is widely used to describe many diverse solid-state materials.[58] The observed 10-layer phase (and the examples of $Sr_2LaFe_3O_8$ and $YBa_2Fe_3O_8$ which have the same composition but different structures due to the differing vacancy distributions) shows the difference between composition and structure (which arises from both the composition *and* the sequence of blocks) in defining homologous series. The simplest way to write the composition of the 10-layer phase here is $(A_2B_2O_5)_n(ABO_3)_m$, with $n = 2$ and $m = 1$, but the identification of two distinct $A_2B_2O_5$ units (one with vacancies at the BO_2 sheet level enforcing tetrahedral/trigonal geometry, and the other in the AO layer to make square pyramids) gives a better description of **III** as $(A'_2B'_2O_5)(A''_2B''_2O_5)(ABO_3)_m$, where m is, in principle, variable. However, even this description does not allow the straightforward identification of cation environments; thus, a more complete description would involve four distinct modules based on AO and BO_2 layers (Figure 10; superscript numbers refer to the crystallographically distinct A and B sites in **III**): $A^3OB^3OA^3O$ (a pseudo-tetrahedral BO layer between two AO layers), $B^1O_2A^1B^1O_2$ (a double layer of BO_2 layers surrounding an 8-coordinate A layer), A^2O layers between non-defective BO_2 layers, and B^2O_2 layers between non-defective AO layers. This gives an overall repeat of $(A^2O)(B^1O_2A^1B^1O_2)(A^2O)(B^2O_2)(A^3OB^3OA^3O)(B^2O_2)$. While more complex than the description initially given, this can give rise to several potential homologous series. The $Ca_2Fe_2O_5$ ($n = 1$) and $Sr_2LaFe_3O_8$ ($n = 2$) (Figure 10a) members of the simple series $\{(A^2O)(B^2O_2)\}_{n\text{-}1}(A^3OB^3OA^3OB^2O_2)$ are known, where n is chosen to match the prevalent numbering scheme for the known phases. $\{(A^2O)(B^1O_2)\}_n\{(A^1)(B^1O_2)\}_m$ ($LaNiO_2$, $m = 1$, $n = 0$; $BaTiO_3$, $n = 1$, $m = 0$; $NdBaFe_2O_5$, $n = 1$, $m = 1$; $YBa_2Fe_3O_8$, $n = 2$, $m = 1$; it is interesting to note that no $m > 1$, $n = 1$ members are known yet) and $\{(B^2O_2)(A^2O)\}_n(B^1O_2A^1B^1O_2)\{(A^2O)(B^2O_2)\}_n(A^3OB^3OA^3O)$ ($n = 0$, $LnSr_2Cu_2GaO_7$, Figure 10b; $n = 1$, **III**, Figure 10c; $n = 2$, member, Figure 10d). There are also yet more complex series combining the above modules: $[\{(A^2O)(B^2O_2)\}_m(A^3OB^3OA^3OB^2O_2)]_n\{(A^2O)(B^2O_2)\}_o[\{(A^1)(B^1O_2)\}_p\{(A^2O)(B^1O_2)\}_q]$, though it is likely m, o, and q will have similar values. The observation of the various inter-growth defects in Figure 9 may well indicate that some of these more complex structures are synthetically attainable.

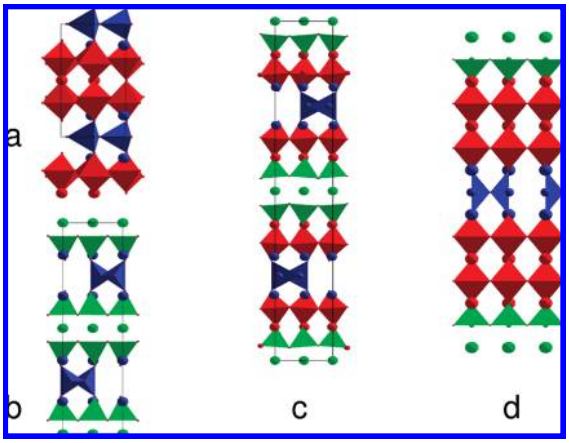

Figure 10. Structures belonging to the homologous series $\{(A^2O)(B^2O_2)\}_{n\text{-}1}(A^3OB^3OA^3OB^2O_2)\}$, (a) $Sr_2LaFe_3O_8$ ($n = 2$), and $\{(B^2O_2)(A^2O)\}_n(B^1O_2A^1B^1O_2)\{(A^2O)(B^2O_2)\}_n(A^3OB^3OA^3O)$, (b) $LnSr_2Cu_2GaO_7$ ($n = 0$), (c) **III** ($n = 1$), and (d) half the unit cell of the hypothetical $14a_p$ ($n = 2$) member. $A^3OB^3OA^3O$ (a pseudo-tetrahedral BO layer between two AO layers) is shown in blue, $B^1O_2A^1B^1O_2$ (a double layer of BO_2 layers surrounding an 8-coordinate A layer) in green, and both A^2O layers between non-defective BO_2 and four B^2O_2 layers between non-defective AO layers in red.

Acknowledgment. We acknowledge the UK EPSRC for support under EP/C511794 (M.A., J.H.) and GR/R36411 (CT), and for access to ESRF (where Dr. F. Fauth and Prof. A. N. Fitch are thanked for assistance on beamline ID31), SRS (where Dr. M. A. Roberts is thanked for assistance on beamline 9.1), ISIS (where Dr. W. A. Kockelmann is thanked for assistance on the GEM diffractometer), and ILL (where Dr. P. F. Henry is thanked for assistance on the D2B and D20 diffractometers). We acknowledge support from the FAME Network of Excellence under the EU Framework VI programme.

Supporting Information Available: Supplementary figures (11) and tables (6) together with crystallographic information files for the refinements for all samples. This material is available free of charge via the Internet at http://pubs.acs.org.

JA077762F

---

(58) Ferraris, G.; Makovicky, E.; Merlino, S. *Crystallography of Modular Materials*; Oxford University Press: New York, 2004.